Dynamic equivalent magnetic network model and drive system of permanent magnet synchronous motor with double V-shaped magnet structure

Wenjing Zhang, Yanliang Xu, Xin Tian, Ngac Ky Nguyen, Eric Semail

Dynamic Equivalent Magnetic Network Model and Drive System of Permanent Magnet Synchronous Motor with Double V-Shaped Magnet Structure

Wenjing Zhang[a], Yanliang Xu[a,]*, Xin Tian[b], ,

[a] *School of Electrical Engineering, Shandong University, Jinan, China*
[b] *State Grid Zhumadian Electric Power Company, Zhumadian, China*
[c] *Laboratory of Electrical Engineering and Power Electronics, University of Lille, Arts et Metiers Institute of Technology, Centrale Lille, Yncrea Hauts-de-France, ULR 2697-L2EP, Lille, France*

A B S T R A C T

In order to improve the driving performance of electric vehicles (EV), a permanent magnet synchronous motor with double V-shaped magnet structure (DVMPMSM) and its driving system are studied in this paper. A 150kW DVMPMSM for EV is designed firstly, and the design parameters of the motor are determined. In order to overcome the drawbacks of the finite element analysis (FEA), especially the issue on calculating time, a dynamic equivalent magnetic network (EMN) model of the DVMPMSM is constructed, by which the air gap flux density, back electromotive force, electromagnetic torque and winding inductance parameters of the motor can be solved. Compared with the FEA, the dynamic EMN model constructed in this paper greatly increases the calculation speed while the calculation accuracy is maintained well. This paper also introduces the stator winding switching method to replace the field-weakening control method. Then, a vector control method of DVMPMSM based on dynamic EMN model and stator winding switching is proposed. The demands brought forward by EV for high torque output under low speed and high upper limit of speed can be well satisfied. Finally, the accuracy of the dynamic EMN model and the effectiveness of the proposed control method is validated through prototype experiments.

1. Introduction

Compared with the traditional fuel automotive, electrical vehicle (EV) abandons the complicated technology of internal combustion engines to simplify the manufacturing of automotive. In addition, EV also combines the advantages of high efficiency and cleanliness, so it is regarded as an ideal substitute for fuel automotive [1]. Typically, an EV is mainly composed of a battery, a drive motor and a supplementary drive system. The motor and its drive system are the core components of EV [2-4]. The motors commonly used in EV mainly include switched reluctance motor, induction motor, and permanent magnet synchronous motor (PMSM) [5-8]. Especially, PMSM has received extensive attention for its ultra-high efficiency and torque density [9-10]. Toyota Pruis has currently launched the fourth generation of PMSM for EV. The first generation of Pruis motor uses a I-shaped magnet structure on the rotor. The second and third generations of Pruis motors use a single V-shaped magnet structure on the rotor which enhances the flux concentrating effect and is conducive to

* *Corresponding author.* Tel.: +0-000-000-0000 ; fax: +0-000-000-0000.
E-mail address: author@institute.xxx
Peer review under responsibility of xxxxx.

improving the torque density. The fourth-generation Pruis motor launched in 2017 adopts a V-I-shaped double-layer magnet structure on the rotor, which increases the reluctance torque. Germany's BMW company launched an insert-type PMSM of which the rotor adopts a double-I shaped magnet structure in 2013. Compared with the single I-shaped rotor magnet structure, it is beneficial to further increase the torque density of the motor. The permanent magnet synchronous motor with a double V-shaped magnet structure (DVMPMSM) which is rarely used and researched in the field of EV so far combines the characteristics of the V-shaped magnet structure and the double-layer magnet structure, thus its torque density is expected to reach even higher.

The equivalent magnetic network (EMN) method is seemed as a more efficient analytical method for the magnetic field in the motors that combines the higher calculation accuracy than the equivalent magnetic circuit method (EMC) [11] and faster calculation speed than the finite element method (FEM). W. Shi, et al. studied the EMN of a PMSM with a V-shaped magnet structure, which can accurately calculate the magnetic field distribution and simulate the anti-demagnetization ability of the motor [12]. J. Zhang et al. proposed a double-layer magnet structure permanent magnet synchronous reluctance motor and established its EMN model which can accurately calculate the air gap flux density distribution of the motor and be used in the design and optimization of the rotor structure [13]. Nevertheless, the EMN model in [12] and [13] is not available for the calculation of the winding flux, electromotive force (EMF) and torque waveforms along with the rotation of the rotor. Then, the dynamic EMN model in which the connection of the EMNs between the stator and rotor is modified according to the rotor position is introduced to deal with this question. H. Kwon et al. researched and established the dynamic EMN model of a PMSM with a surface-inset magnet structure, which can obtain similar magnetic field calculation results as FEM [14]. G. Liu, et al. studied the dynamic EMN model of a PMSM with a single-layer V-shaped magnet structure. Its correctness was validated by FEM and experiments [15]. In [16], a dynamic EMN model is used for the multiobjective optimization of a surface-mounted PMSM which is beneficial for the fast design of the motor. However, there are no related researches about the dynamic EMN model for the proposed DVMPMSM which is investigated in this paper.

For EV, the maximal driving speed mainly depends on the speed range of the motor which is limited by the DC bus voltage [17]. In order to extend the speed-range of the motor, field-weakening control (FW) is generally used [8] [18-20]. However, there are some inevitable problems when using FW to increase the speed maximum of the motor. Firstly, the output electromagnetic torque will rapidly decrease as the speed increases. In addition, it will increase the loss of the motor drive system, and even cause local irreversible demagnetization of permanent magnets while using FW [21]. The winding switching operation is to change the connection mode and number of the parallel branches through the switching components. Its purpose is to solve the contradiction between the large torque and high speed, and effectively overcome the defects of the speed extension using FW method [22]. The related academic researches on winding switching mainly focus on the changes in motor performance before and after switching, and the dynamic process during switching [23-24]. In [25], a novel winding reconfiguration circuit topology for a V-shape interior permanent magnet synchronous motor is proposed. The operating range can be extended effectively through changing the connections of winding and the surge voltage can be prevented using the proposed circuit topology. In [26], the winding switching technology is applied to extend the speed-range of an in-wheel PMSM with high efficiency. In [27], the winding switching characteristics on the driving permanent magnet brushless direct current motor (BDCM) are studied. Based on the above researches, it can be concluded that the EV's acceleration ability under high speed can be improved and the maximal torque under low-speed or the maximal velocity of EV can be enhanced largely through the adoption of winding switching.

In this paper, a 150kW DVMPMSM is designed according to the application requirements of commercial trucks first of all. In order to shorten the analysis and calculation process of DVMPMSM while ensuring the accuracy of calculation, this paper establishes a dynamic EMN model for DVMPMSM. In addition, a vector control method for DVMPMSM based on dynamic parameters database and stator winding switching is proposed to satisfy the requirement of EV for low-speed, high-torque and large speed-range. Finally, a 150kW prototype is manufactured and the no-load as well as load experiments are both conducted.

2. Design of DVMPMSM

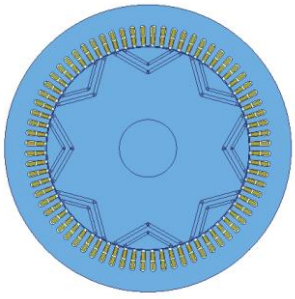

Fig. 1. Two-dimensional structure diagram of the 150kW DVMPMSM.

Compared with other rotor magnet structures such as single V-shaped and double I-shaped, the double V-shaped rotor magnet structure enjoys better flux-concentrating ability. Thus, higher torque density and overload capacity can be achieved for DVMPMSM which is beneficial to promote its application in EV and other fields. Based on the application background of a small commercial truck, a DVMPMSM with a rated power of 150kW is designed.

Fig. 1 shows the two-dimensional structure diagram of the 150kW DVMPMSM. A combination of 72-slot 8-pole is adopted. The main design parameters of the motor are shown in TABLE. 1.

Table 1

The main design parameters of DVMPMSM.

Parameter	Value
Rated power	150kW
Rated speed	3000r/min
Rated voltage	380V
Outer diameter of stator	400mm
Inner diameter of stator	285mm

Axial length	193mm
Width of slot open	3.8mm
Winding type	Double layer lap winding
Length of air gap	1.6mm
Outer diameter of rotor	281.8mm
Inner diameter of stator	130mm

3. Dynamic EMN Model of DVMPMSM

3.1. Construction of Dynamic EMN model

The magnetic circuit of the PMSM can be divided into three parts, namely the stator magnetic circuit, the rotor magnetic circuit and the air gap magnetic circuit, respectively. Therefore, the EMN models of these three parts are constructed firstly.

The pole-slot combination of DVMPMSM is 72-slot 8-pole. In order to reduce the calculation time, only a pair of magnetic poles, namely the 18-slot 2-pole EMN model is established according to the symmetry of the total magnetic circuit.

It can be considered that the flux density of stator tooth is constant along radial direction when constructing the EMN model of the stator. Thus, each stator tooth can be equivalent to one reluctance of which value is determined by (1). The schematic diagram of the stator yoke between two adjacent stator teeth is shown in Fig. 2. The length between the two dotted arcs shown in Fig. 2 is dx, and the permeance of this part can be calculated using (2). Finally, the permeance of the stator yoke can be obtained by integrating (2), and the calculation result is shown as (3).

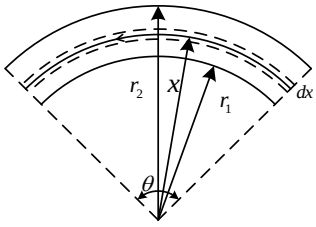

Fig. 2. The schematic diagram of the stator yoke.

$$R=\frac{L}{\mu_r\mu_0 s}, \tag{1}$$

where L is the height of stator teeth, s is the cross-sectional area of single tooth described as the product of the width and axial length of tooth.

$$dg_e=\frac{u_{se}l_{ef}}{\theta x}dx, \tag{2}$$

$$G_{se}=\int_{r1}^{r2} dg_e \quad \int_{r1}^{r2}\frac{u_{se}l_{ef}}{\theta x}dx=\frac{u_{se}l_{ef}}{\theta}ln\frac{r_2}{r_1}, \tag{3}$$

where u_{se} is the permeability of the stator yoke, l_{ef} is the axial length of the stator.

The distribution diagram of the three-phase armature windings under a pair of magnet poles is shown in Fig. 3. The phases are represented by a, b, and c, respectively. Under load conditions, the current is input to armature coils and flows into each conductor. The direction of the current is represented by $\times$ and $\bullet$ as shown in Fig. 3 where × indicates the current flows into vertically and $\bullet$ indicates the current flows out vertically. In order to consider the influence of the armature current on the magnetic field of air gap, the stator armature current is equivalent to the source of magnetomotive force located on the stator yoke, according to the Ampere Loop Theorem. The stator yoke part between two adjacent stator teeth is equivalent to a magnetic flux tube and a source of magnetomotive force in series. The equivalent source of magnetomotive force located on each yoke can be obtained by (4).

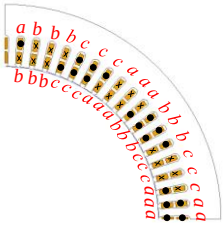

Fig. 3. The distribution of the three-phase armature winding.

$$\begin{cases} f_{se1}=2i_{a+} \\ f_{se2}=i_{a+}+i_{c-} \\ f_{se3}=2i_{c-} \\ f_{se4}=2i_{c-} \\ f_{se5}=i_{b+}+i_{c-} \\ f_{se6}=2i_{b+} \\ f_{se7}=2i_{b+} \\ f_{se8}=i_{a-}+i_{b+} \\ f_{se9}=2i_{a-} \\ f_{se10}=2i_{a-} \\ f_{se11}=i_{c+}+i_{a-} \\ f_{se12}=2i_{c+} \\ f_{se13}=2i_{c+} \\ f_{se14}=i_{b-}+i_{c+} \\ f_{se15}=2i_{b-} \\ f_{se16}=2i_{b-} \\ f_{se17}=i_{a+}+i_{b-} \\ f_{se18}=2i_{a+} \end{cases}, \tag{4}$$

where f_{sen} is the magnetomotive source of n_{th} stator yoke part.

The air gap reluctances of different regions are non-uniform because of the existence of the stator cogging, resulting in the distortion of the air gap flux density waveform. The slot open area is equivalent to two slot open reluctances serially. The reluctance of each one is obtained by (5), where l_{gs} represents half of the slot width, and s_{gs} is the product of the slot height and the axial length l_{ef}.

$$R_{gs}=\frac{l_{gs}}{\mu_0 s_{gs}} \tag{5}$$

Finally, an EMN model of the stator as shown in Fig. 4 can be obtained, including 18 stator slot reluctances, 18 stator yoke reluctances, 18 equivalent magnetomotive sources and 36 slot open reluctances.

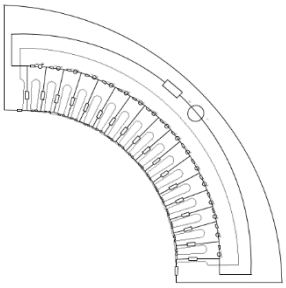

Fig. 4. EMN model of stator.

In order to consider the influence of the slot open on the air-gap flux density waveform, this paper modeled the air-gap reluctances corresponding to the stator teeth and slots respectively. Assuming that the cross-section area of the magnetic circuit of the air gap along the radial direction is equal to the area corresponding to the average air gap, the air gap reluctance corresponding to the stator tooth R_{gt} and the air gap reluctance corresponding to the stator slot R_{gg} are calculated by the following equations:

$$R_{gt}=\frac{l_g}{\mu_0 s_{gt}}, \tag{6}$$

$$R_{gg}=\frac{l_g}{\mu_0 s_{gg}}, \tag{7}$$

where l_g indicates the length of air gap which can be calculated by (8). s_{gg} and s_{gt} indicate the cross-section area of the magnetic circuit corresponding to the tooth and the slot open respectively. s_{gg} and s_{gt} are calculated via equations (9)-(10).

$$l_g=\frac{\left(D_{dn}-D_{zw}\right)}{2}, \tag{8}$$

$$s_{gg}=\frac{b_g}{b_t+b_g}s_g, \tag{9}$$

$$s_{gt}=\frac{b_t}{b_t+b_g}s_g, \tag{10}$$

where b_g and b_t indicate the width of the slot open and the tooth respectively.

$$s_g=\pi\times\left(D_{dn}\quad D_{zw}\right)l_{ef}\ /144, \tag{11}$$

where D_{dn} is the inner diameter of the stator, D_{zw} is the outer diameter of the rotor.

For the double V-shaped magnet, the upper magnet is divided into four parts, downer magnet is divided into six parts. The magnetic flux barriers are designed located at the terminal of the magnet. The EMN model of the rotor part is shown in Fig. 5. The rotor magnets are described as the source of magnet flux. The flux and reluctances of EMN model can be calculated according to (12)-(13).

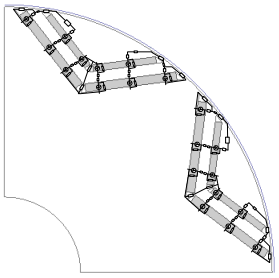

Fig. 5. The EMN model of rotor magnets and magnet flux barriers.

$$\Phi_0=B_{r0}\times s, \tag{12}$$

$$R_0=\frac{h_m}{\mu_r\mu_0 s}, \tag{13}$$

where B_{r0} is the remanence of the permanent magnet, s is the surface area of magnet, μ_r is the relative permeability of permanent magnet and h_m is the thickness of the magnet.

Divide the rest of the rotor and the EMN model of the rotor can be obtained shown in Fig. 6. The blue reluctances shown in Fig. 6 are corresponding to the surface of the rotor.

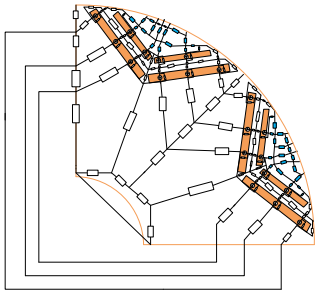

Fig. 6. EMN model of the rotor.

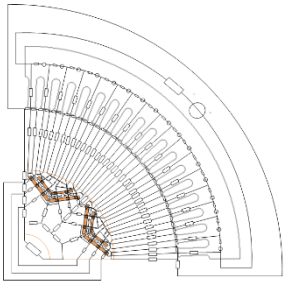

Fig. 7. Static EMN model of DVMPMSM.

The total static EMN model can be constructed by combining EMN models of both stator and rotor. The total EMN model of DVMPMSM is shown in Fig. 7. During the rotation of the rotor, the relative position between stator and rotor will be renewed continuously. Thus, all the nodes connected to the air gap reluctance branch and the rotor reluctance branch in the static EMN model of DVMPMSM are deleted firstly while the rotor position is changed. Then the rotor reluctance branch and the air gap reluctance branch will be reconnected to establish an EMN model for new rotor position. The above procedures must be repeated after the rotor rotates to a new position to establish a dynamic EMN model of DVMPMSM.

3.2. Construction and Solution of Nonlinear Equations of EMN model

When the rotor rotates to a certain position, there will be a static EMN model corresponding to it. It can be seen from Fig. 7 that the entire static EMN model contains 138 nodes. One of the nodes is selected as the reference node and then the nonlinear equations based on the magnetic potential of the node are established which consists of 137 independent equations.

The equations contain lots of ferromagnetic reluctance terms, the value of which is uncertain and related to its permeability. In order to solve these nonlinear equations, the secant method characterized by excellent ability on iterative calculation is used in this paper.

The secant method is described in Fig. 8. Assuming that the magnetic field intensity obtained from the kth iteration is H_k and the magnetic flux density is B_{ca}^k. Then μ_r^k can be calculated by (14), which corresponds to point A shown in Fig. 8. It can be seen that point A deviates greatly from the magnetization curve and the accuracy of the solution can not be satisfied. Thus the next iteration needs to be performed. According to the magnetization curve of the ferromagnetic material, the interpolation result at H_k is B_{it}^k, which corresponds to point B shown in Fig. 8. And then the permeability μ_r^{k+1} required for the $(k+1)_{\text{th}}$ iteration is calculated using (15). Normally, the calculation result can be considered as convergent in the k+1 iteration calculation if the permeability of all ferromagnetic reluctances in the EMN model satisfy (16).

$$\mu_r^k = \frac{B_{ca}^k}{H^k \mu_0}, \tag{14}$$

$$\mu_r^{k+1} = \frac{B_{it}^k}{H^k \mu_0}, \tag{15}$$

$$\left| \frac{\mu_r^{k+1} - \mu_r}{\mu_r^k} \right| < \varepsilon, \tag{16}$$

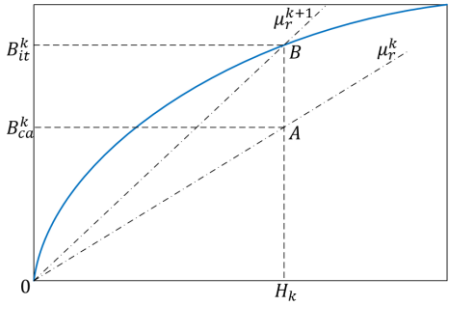

Fig. 8. Diagram of secant method.

The modeling and solution process of the dynamic EMN model is shown in Fig. 9. While the rotor reaches a new position, the initial value of the permeability of each reluctance is re-assigned, and the initial permeability matrix of the nodal magnetic potential equations is obtained according to the EMN model re-constructed. Then the magnetic potential of each node is calculated iteratively by the secant method shown in Fig. 8. The flux density flowing into each reluctance is calculated by Ohm's law of the magnetic circuit. Finally, the magnetic field distribution inside the motor and the electromagnetic performances of the motor are calculated.

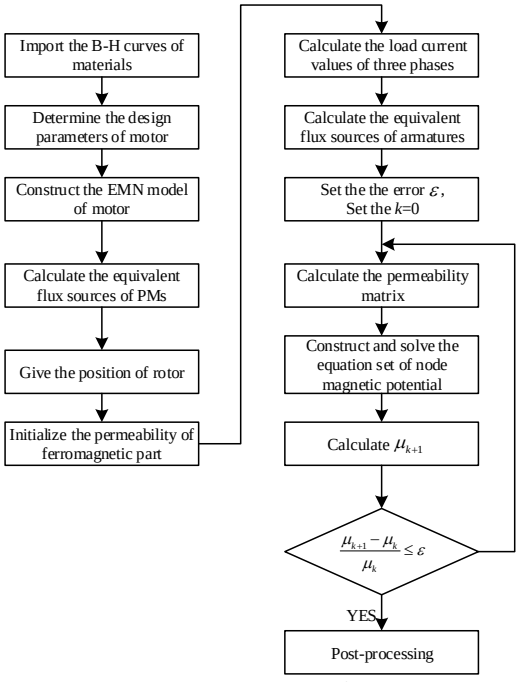

Fig. 9. The modeling and solution process of the dynamic EMN model.

3.3. Validation of Dynamic EMN Model

Under no-load condition, the EMN method and the finite element method are both used to calculate the air gap magnetic density waveform as shown in Fig. 10. It can be seen that the no-load air gap flux density waveform is approximately flat-top, and it is distorted by the stator slot leakage reluctances increasing its harmonic content. The amplitude of the air gap flux density calculated by the FEM is 1.133T, while the result calculated by the EMN method is 1.093T. It can be seen that the result calculated by EMN method is consistent well with the result obtained by FEM. The accuracy of the EMN method is validated.

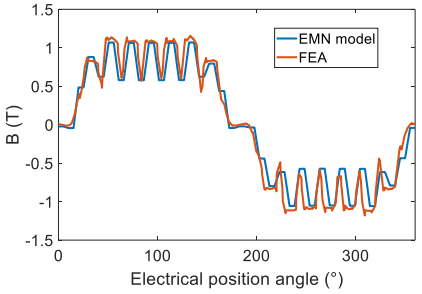

Fig. 10. The comparison of air gap flux density obtained by EMN method and FEM under no load condition.

The comparison of the no load winding flux-linkage waveforms calculated by the EMN method and FEM are shown in Fig. 11 while the number of parallel branches is set to 4. It can be seen that the waveforms of the flux linkage calculated by these two methods are approximately sinusoidal and almost coincide. The amplitude of the no-load flux-linkage calculated by the EMN method is 0.2562Wb, and it is 0.2669Wb for

calculated by FEM. The result of the EMN method is 4.0% lower than that of the FEM.

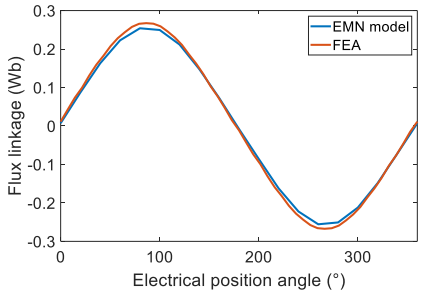

Fig. 11. The comparison of flux-linkage waveforms obtained by EMN method and FEM under no load condition.

The electromotive force (EMF) of windings can be calculated by using (17). The comparison of one phase EMF waveforms calculated by the EMN method and the FEM are shown in Fig. 12 while the motor speed is set to 3000r/min and the number of parallel branches is set to 4. It can be seen that the result obtained by EMN agrees well with that of FEM.

$$e=\frac{\Psi_{1}-\Psi_{i-1}}{2h}, \tag{17}$$

where h indicates the time difference between two adjacent rotor positions.

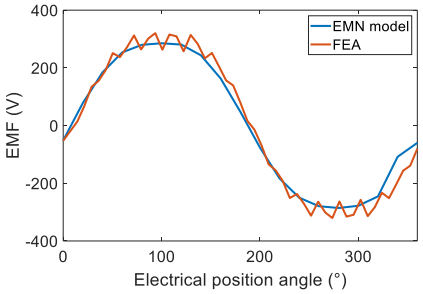

Fig. 12. The comparison of EMF waveforms.

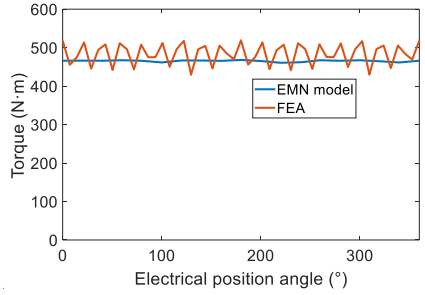

Fig. 13. The electromagnetic torque waveforms calculated by the EMN method and FEM.

The number of parallel branches of the motor is set to 4, and the given load current is set to i_d=-50.5A and i_q=305A. The electromagnetic torque waveforms calculated by the EMN method and FEM are shown in Fig. 13. The average value of electromagnetic torque is 465.3Nm while using the EMN method and it is 483.7Nm while using FEM. It can be calculated that the relative error between the two results is 3.8%.

4. Vector Control Method based on Dynamic Parameters Database and Stator Winding Switching Method

4.1. Operation under Stator Winding Switching

In general, the electromagnetic torque will rapidly decrease as the speed increases, in addition, the speed range will be limited while FW is used to extend speed range. Besides, the loss of the drive system will rise and then the permanent magnets will appear locally irreversible demagnetization. In this paper, the stator winding switching method is used to improve the electromagnetic torque of DVMPMSM under low speed and to expend its speed range. The speed range of DVMPMSM is assigned to 3 gears as given in Table 2.

Table 2

The three gears assigned to DVMPMSM.

Gear	**1**	**2**	**3**
Range of speed (RPM)	0-1500	1500-3000	3000-6000
Number of parallel branches	2	4	8

The speed-torque diagrams of both winding switching method and FW method are shown in Fig. 14 while a constant input current is guaranteed. It can be seen that these two speed-torque curves are overlapped while the speed is lower than 1500 RPM. While the speed is increased furtherly, the torque decreases rapidly in FW method, and the extension of speed is limited. In winding switching method, the speed range of motor is doubled and the output torque is halved as the number of parallel winding branches is doubled.

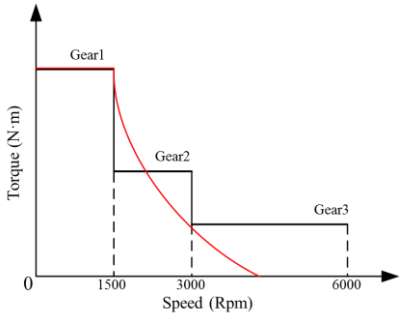

Fig. 14. Torque-speed diagram.

4.2. Establishment of Dynamic Parameters Database

In order to shorten the simulation process and save computing resources, the method of offline calculation is adopted in this paper. The permanent magnet flux linkage, quad-axis and direct-axis synchronous inductance under different winding connections and different loads are calculated by the dynamic EMN model to establish a database of motor dynamic parameters. As a result, the motor parameters under different operating conditions can be selected in the database to modify the DVMPMSM model in real-time.

The permanent magnet flux linkage of DVMPMSM will change after completing once winding switching. The three-phase winding flux linkage can be calculated by the dynamic EMN model, and then the permanent magnet flux linkage can be calculated according to (18). The permanent magnet flux linkage waveforms of DVMPMSM with 2, 4, and 8 parallel branches are shown in Fig. 15.

$$\Psi_f = \frac{2}{3}\left(\Psi_a \times \cos\theta + \Psi_b \times \cos\left(\theta - 2\pi \quad 3\right) + \Psi_c \times \cos\left(\theta - 4\pi / 3\right)\right), \tag{18}$$

where θ is the position angle of the rotor.

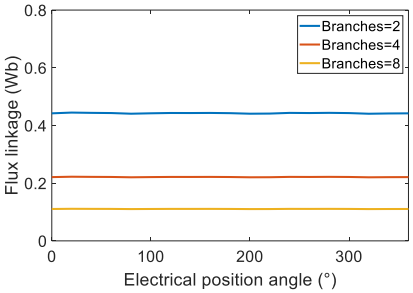

Fig. 15. Torque-speed diagram.

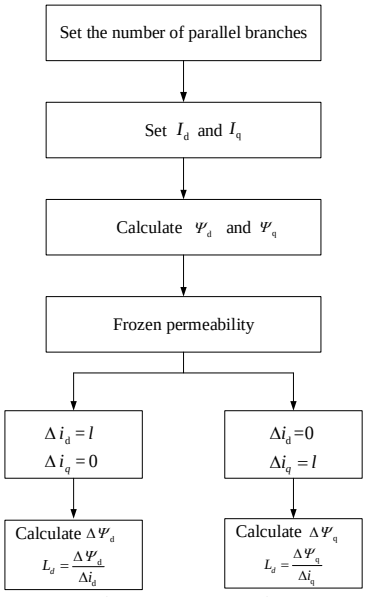

Fig. 16. The procedures of the calculation of the quad- and direct- axis synchronous inductances.

In order to construct a more complete motor dynamic parameter database for the DVMPMSM model that considers the overload operation, the direct- and quad- axis synchronous inductance within the range of twice the rated current are calculated by the dynamic EMN model. After completing winding switching once, its direct- and quad-axis synchronous inductance will change. The dynamic EMN model is used to calculate the direct- and quad- axis synchronous inductance with different parallel branches and under different loads. And then those parameters are stored in the dynamic parameter database providing corresponding parameters of DVMPMSM under different gears and loads. The procedures of the calculation of the quad- and direct- axis synchronous inductances using the dynamic EMN model are given in Fig. 16.

When the branches in parallel is set for 4, the variation of the direct-axis and quad-axis synchronous inductances with different combinations of direct- axis and quad- axis current is shown in Fig. 17. It can be seen that the direct-axis synchronous inductance remains almost constant with the variation of the load current. The quad-axis synchronous inductance of the motor slightly increases with the increase of the direct-axis demagnetization current. However, the saturation of the quad-axis magnetic circuit of the DVMPMSM greatly increases as increasing quad-axis current.

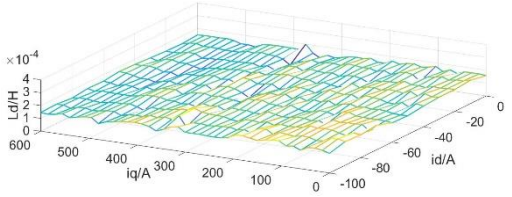

(a) Direct-axis

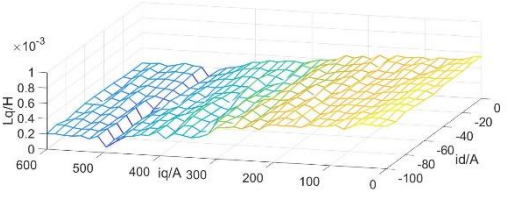

(b) Quad-axis

Fig. 17. The variation of synchronous inductances with the load current (2a=4).

When the number of parallel branches of the stator winding is set to 2 and 8, the variations of the direct- and quad-axis synchronous inductances with the load current are shown in Fig. 18 and Fig. 19, respectively.

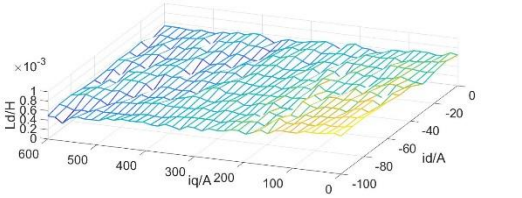

(a) Direct-axis

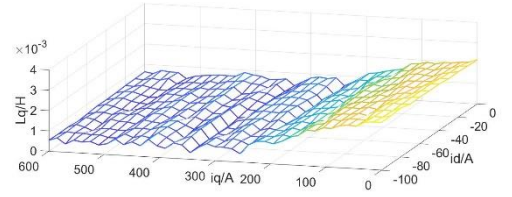

(b) Quad-axis

Fig. 18. The variations of the synchronous inductances with the load current (2a=2).

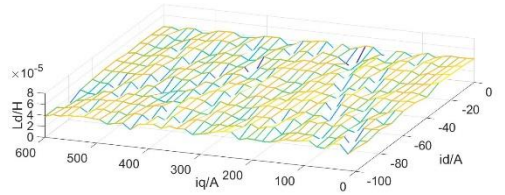

(a) Direct-axis

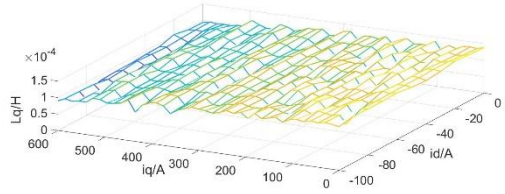

(b) Quad-axis

Fig. 19. The variations of the synchronous inductances with the load current (2a=8).

4.3. The Vector Control Method and its Simulation Results

The principle of the vector control method based on the dynamic parameters database and winding switching (VC-DPD&WS) is shown in Fig. 20. The maximum torque per ampere (MTPA) control strategy is adopted in the control model. During the simulation, the number of parallel branches is adjusted according to the speed of the motor. In addition, the parameters of the DVMPMSM are modified using dynamic parameters database in real-time, including the permanent magnet flux linkage, winding resistance, direct- and quad-axis synchronous inductances.

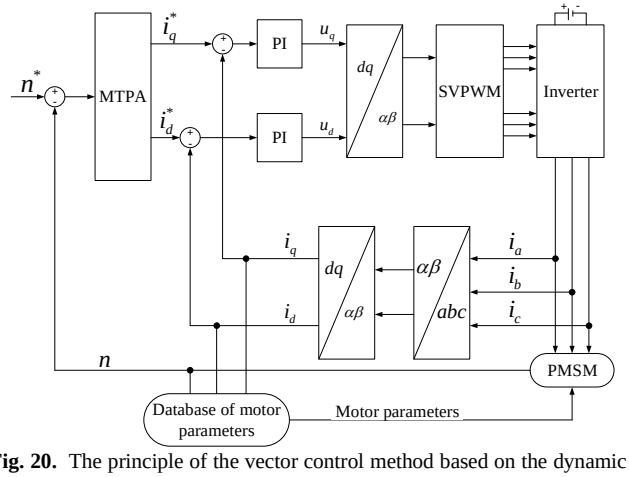

Fig. 20. The principle of the vector control method based on the dynamic EMN model and the stator winding switching.

The software MATLAB is used to construct a control model for DVMPMSM. The total simulation time is set to 1.2s, the load torque is set to 100Nm. The given speed waveform and the simulated speed waveform are shown in Fig. 21.

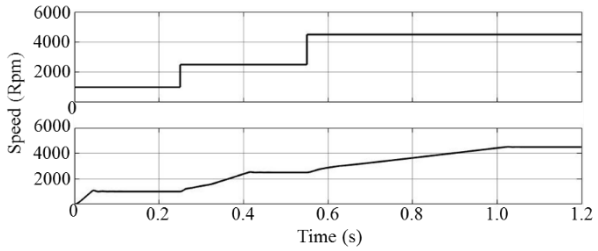

Fig. 21. The comparison of speed waveforms between given and simulated.

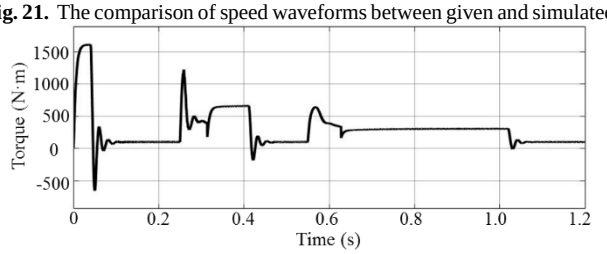

Fig. 22. The waveform of electromagnetic torque.

The electromagnetic torque waveform of DVMPMSM simulated by MATLAB is shown in Fig. 22. The corresponding three-phase stator current waveform during the simulation is shown in Fig. 23. The steady-state current amplitude is 32A while the motor speed is set to 1000 r/min. While the motor speed is set to 2500 r/min and 4500 r/min, the corresponding steady-state current amplitudes are 66A and 134A respectively. It can be concluded that the stator current of the motor in the third gear is basically twice that in the second gear and 4 times that in the first gear under the condition of outputting the same electromagnetic torque.

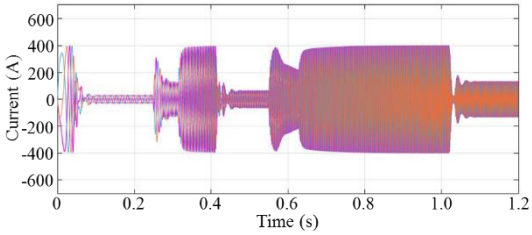

Fig. 23. The waveform of three-phase current.

As shown in Fig. 24, the stepped load torque is given while the speed of the motor is set as shown in Fig. 21(a). The three-phase stator current waveform of the motor is shown in Fig. 25. It can be seen that the amplitude of the three-phase stator current when the motor reaches a steady-state under various load torques is almost same.

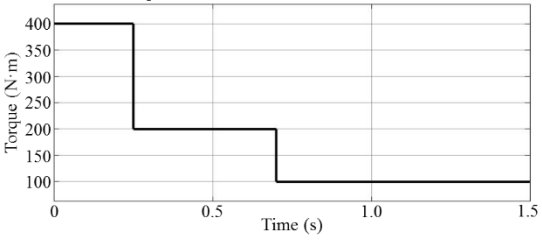

Fig. 24. The waveform of stepping load torque.

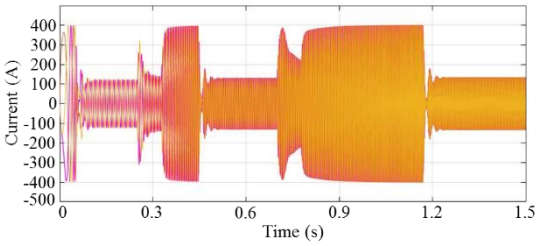

Fig. 25. The waveform of three-phase stator current.

It can be concluded that the DVMPMSM can output large torque under low speed by using VC-DPD&WS. In addition, the maximal speed of the motor can be multiplied with the rise of gear under the constant DC bus voltage. However, it should be considered that the maximal output torque of DVMPMSM will decrease exponentially with the rise of gear due to the limitation of DC bus current.

5. Prototype and Experiment

As shown in Fig. 26, an experimental platform is built in order to test the prototype DVMPMSM proposed in this paper. The experimental platform is mainly composed of a prototype, a dynamometer, a load motor, a water-cooling system, a motor controller and a low-voltage DC power supply. The motor controller is set up based on Infineon TC1797 which can realize vector control and stator winding switching.

The no-load line back-EMF waveform of the prototype under the speed of 1500r/min is shown in Fig. 27(a) under the 1st gear. The no-load line back-EMF waveform of the prototype under the speed of 3000r/min is shown in Fig. 27(b) under the 2nd gear. The no-load line back-EMF waveform of the prototype under the speed of 5500r/min is shown in Fig. 27(c) under the 3rd gear. It can be seen that the magnitudes of the back-EMF at the above three given speeds are almost equal. It can be concluded that the linear increase of the back-EMF can be effectively inhibited through the stator winding switching resulting from the reduction of the number of turns per phase in series, and so a higher maximum motor speed can be obtained under limited DC bus voltage.

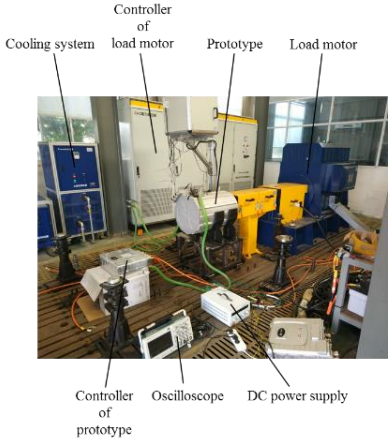

Fig. 26. The experimental platform for DVMPMSM.

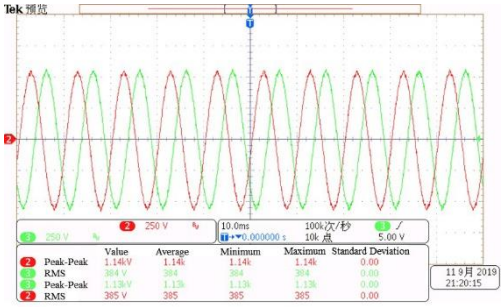

(a) 1500 r/min

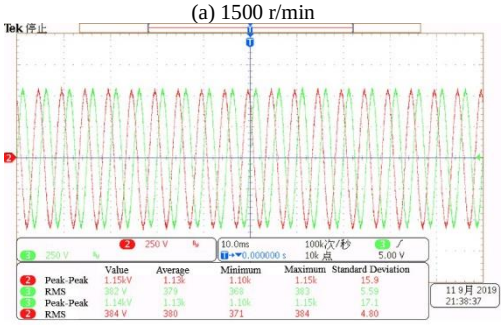

(b) 3000 r/min

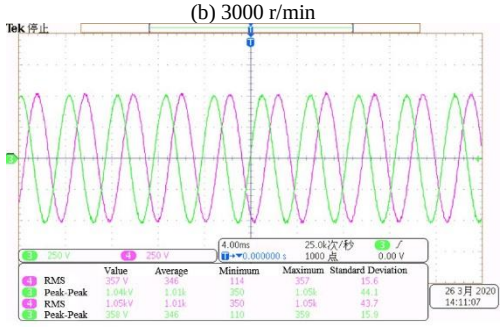

(c) 5500 r/min

Fig. 27. The no-load line back-EMF of the prototype.

While the stator winding is set to the 1st gear, the root means square (RMS) of the no-load line back-EMF of the prototype is measured by the experimental platform and compared with the calculation results of the dynamic EMN model as shown in Fig. 28. The relative error between these two results is within 5%. The accuracy of the dynamic EMN model is verified.

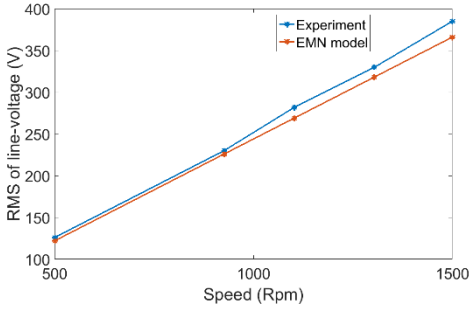

Fig. 28. The comparison of RMS of no-load line back-EMF.

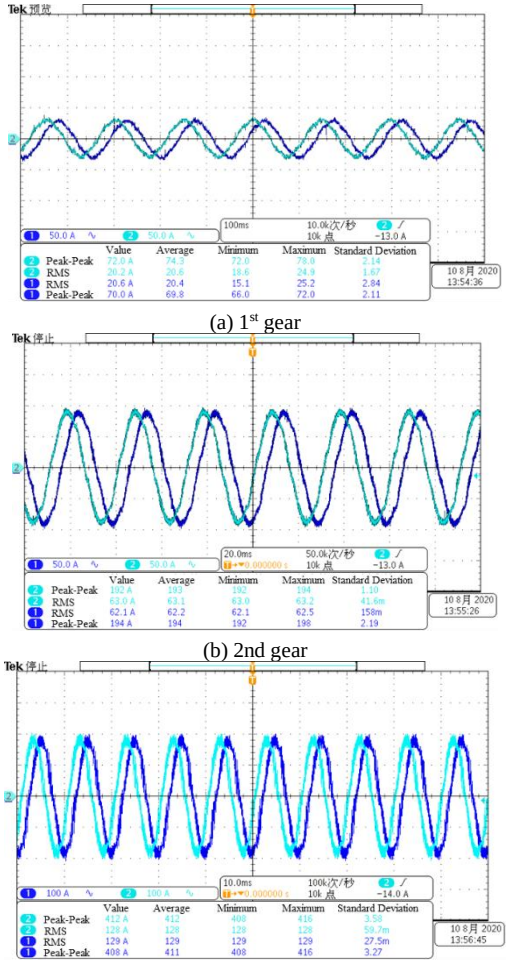

(a) 1st gear

(b) 2nd gear

(c) 3rd gear

Fig. 29. Load current waveforms of the prototype.

In order to investigate the load characteristics of DVMPMSM, the load torque is set to 180Nm. When the prototype is set to the 1st gear and the speed is set to 1000r/min, its stator current is shown in Fig. 29(a) from which it can be calculated that the current amplitude is 36.0A. When the prototype is set to the 2nd gear and the speed is set to 2500r/min, its load current is shown in Fig. 29(b) from which it can be calculated that the current amplitude is 96.5A. When the prototype is set to the 3rd gear and the speed is set to 4500r/min, its load current is shown in Fig. 29(c) from which it can be calculated that the current amplitude is 206.0A. Finally, it can be concluded that a highest maximal output torque can be obtained at low speed under the same limited DC bus current.

6. Conclusion

In this paper, a DVMPMSM for EV is designed. The EMN method is used to calculate its internal magnetic field distribution. In addition, a vector control method based on stator winding switching is proposed according to the requirements of EV for power. Through the research in this paper, the following conclusions are drawn:

(1) The air gap flux density is improved by adopting the double V-shaped magnet structure. Besides, the resistance torque can be improved.

(2) The dynamic EMN model of the DVMPMSM with 18 slots and 2 poles is established by which the calculation of the air gap flux density, three-phase winding flux linkage, back-EMF, and electromagnetic torque is realized. The calculation results of the dynamic EMN model are well consistent with the FEA method. The accuracy of the dynamic EMN model is validated. The relative error of the no-load back-EMF between calculated by dynamic EMN model and experiment is about 5%.

(3) The output electromagnetic torque at the 1st gear (low-speed gear) is twice and four times that at the 2nd (medium-speed gear) and 3rd (high-speed gear) gears respectively under the same DC bus current by using VC-DPD&WS. The maximal speed can be doubled with the rise of gear under the same DC bus voltage.

Acknowledgements

This work was supported by the Science and Technology Major Project of Inner Mongolia Autonomous Region (2020ZD0014) and the China Scholarship Council.

References

[1] Park, Min-Ro, et al. "High energy efficiency oriented-control and design of WFSM based on driving condition of electric vehicle." Mechatronics, 81 (2022): 102696.

[2] A. Emadi, Y. J. Lee and K. Rajashekara, "Power Electronics and Motor Drives in Electric, Hybrid Electric, and Plug-In Hybrid Electric Vehicles," in IEEE Transactions on Industrial Electronics, vol. 55, no. 6, pp. 2237-2245, June 2008, doi: 10.1109/TIE.2008.922768.

[3] K. Rajashekara, "Present Status and Future Trends in Electric Vehicle Propulsion Technologies," in IEEE Journal of Emerging and Selected Topics in Power Electronics, vol. 1, no. 1, pp. 3-10, March 2013, doi: 10.1109/JESTPE.2013.2259614.

[4] V. Ivanov, D. Savitski and B. Shyrokau, "A Survey of Traction Control and Antilock Braking Systems of Full Electric Vehicles With Individually Controlled Electric Motors," in IEEE Transactions on Vehicular Technology, vol. 64, no. 9, pp. 3878-3896, Sept. 2015, doi: 10.1109/TVT.2014.2361860.

[5] J. Dong, Y. Huang, L Jin and H. Lin. Review on High Speed Permanent Magnet Machines Including Design and Analysis Technologies [J]. Proceedings of the CSEE, 2014, 34(27): 4640-4653.

[6] Ke Li,Yi Wang. Maximum Torque per Ampere(MTPA) Control for IPMSM Drives Using Signal Injection and an MTPA Control Law[J]. IEEE Transactions on Industrial Informatics,2019,15(10):5588-5598.

[7] J. Mei, Y. Zuo, C. H. T. Lee and J. L. Kirtley, "Modeling and Optimizing Method for Axial Flux Induction Motor of Electric Vehicles," in IEEE Transactions on Vehicular Technology, vol. 69, no. 11, pp. 12822-12831, Nov. 2020, doi: 10.1109/TVT.2020.3030280.

[8] J. Zhu, K. W. E. Cheng, X. Xue and Y. Zou, "Design of a New Enhanced Torque In-Wheel Switched Reluctance Motor With Divided Teeth for Electric Vehicles," in IEEE Transactions on Magnetics, vol. 53, no. 11, pp. 1-4, Nov. 2017, Art no. 2501504, doi: 10.1109/TMAG.2017.2703849.

[9] Yin, Shen, and Wei Wang. "Study on the flux-weakening capability of permanent magnet synchronous motor for electric vehicle." Mechatronics, 38 (2016): 115-120.

[10] Riel, Thomas, et al. "Noise analysis and efficiency improvement of a pulse-width modulated permanent magnet synchronous motor by dynamic error budgeting." Mechatronics, 50 (2018): 225-233.

[11] Krämer, Christian, Andreas Kugi, and Wolfgang Kemmetmüller. "Modeling of a permanent magnet linear synchronous motor using magnetic equivalent circuits." Mechatronics, 76 (2021): 102558.

[12] Shi Wei, Zhang Zhouyun and Zhang Yunhuan, "Anti-demagnetization modeling of interior permanent magnet motor by bidirectional magnetic network," 2014 IEEE Conference and Expo Transportation Electrification Asia-Pacific (ITEC Asia-Pacific), 2014, pp. 1-6, doi: 10.1109/ITEC-AP.2014.6940845.

[13] J. Zhang, J. Wang, Z. Yu and Y. Li, "Analytical Calculation for Two Layers PMSRM based on Equivalent Magnetic Network Method," 2020 IEEE International Conference on Applied Superconductivity and Electromagnetic Devices (ASEMD), 2020, pp. 1-2, doi: 10.1109/ASEMD49065.2020.9276044.

[14] H. Kwon, H. Yeo, S. Jung and H. Jung, "Modelling surface-inset permanent magnet machines by magnetic circuit network model," 2016 19th International Conference on Electrical Machines and Systems (ICEMS), 2016, pp. 1-4.

[15] G. Liu, Y. Wang, Q. Chen, G. Xu and D. Cao, "Design and Analysis of a New Equivalent Magnetic Network Model for IPM Machines," in IEEE Transactions on Magnetics, vol. 56, no. 6, pp. 1-12, June 2020, Art no. 8101112, doi: 10.1109/TMAG.2020.2987546. .

[16] D. Cao, W. Zhao, J. Ji and Y. Wang, "Parametric Equivalent Magnetic Network Modeling Approach for Multiobjective Optimization of PM Machine," in IEEE Transactions on Industrial Electronics, vol. 68, no. 8, pp. 6619-6629, Aug. 2021, doi: 10.1109/TIE.2020.3005105.

[17] J. Su, R. Gao and I. Husain, "Model Predictive Control Based Field-Weakening Strategy for Traction EV Used Induction Motor," in IEEE Transactions on Industry Applications, vol. 54, no. 3, pp. 2295-2305, May-June 2018, doi: 10.1109/TIA.2017.2787994.

[18] E. Trancho et al., "PM-Assisted Synchronous Reluctance Machine Flux Weakening Control for EV and HEV Applications," in IEEE Transactions on Industrial Electronics, vol. 65, no. 4, pp. 2986-2995, April 2018, doi: 10.1109/TIE.2017.2748047.

[19] S. Duan, L. Zhou and J. Wang, "Flux Weakening Mechanism of Interior Permanent Magnet Synchronous Machines With Segmented Permanent Magnets," in IEEE Transactions on Applied Superconductivity, vol. 24, no. 3, pp. 1-5, June 2014, Art no. 0500105, doi: 10.1109/TASC.2013.2280847.

[20] T. Lee, M. Seo, Y. Ko, Y. Kim and S. Jung, "Electromagnetic Performances Analysis of IPMSM According to the Current Control Method Under Flux-Weakening Control Region," in IEEE Transactions on Applied Superconductivity, vol. 28, no. 3, pp. 1-6, April 2018, Art no. 5204806, doi: 10.1109/TASC.2018.2798628.

[21] Q. Li, T. Fan, X. Wen and P. Ning, "An Analytical Approach to Magnet Eddy-Current Losses for Interior Permanent-Magnet Synchronous Machines During Flux Weakening," in IEEE Transactions on Magnetics, vol. 51, no. 8, pp. 1-9, Aug. 2015, Art no. 8107109, doi: 10.1109/TMAG.2015.2423267.

[22] S. Hemmati and M. Barigh, "A new approach for field weakening in a surface mounted permanent magnet synchronous motor by winding switching *," 2019 27th Iranian Conference on Electrical Engineering (ICEE), 2019, pp. 509-514, doi: 10.1109/IranianCEE.2019.8786367.

[23] Y. Wang, Y. Sun, Y. Dun, G. Chen, Q. Yang and X. Zhang, "Winding Switching Simulation of Dual-Stator Permanent Magnet Synchronous Motor for Electric Vehicles," 2018 International Conference on Advanced Mechatronic Systems (ICAMechS), 2018, pp. 262-265, doi: 10.1109/ICAMechS.2018.8506995.

[24] Ji-Young Lee, Byoung-Kuk Lee, Tao Sun, Jung-Pyo Hong and Woo-Taik Lee, "Dynamic analysis of toroidal winding switched reluctance motor driven by 6-switch converter," in IEEE Transactions on Magnetics, vol. 42, no. 4, pp. 1275-1278, April 2006, doi: 10.1109/TMAG.2006.871933.

[25] Y. Sakai, H. Hijikata, K. Akatsu, Y. Miyama and H. Arita, "Study of switching method for MATRIX motor realizing variable characteristic," 2016 IEEE 8th International Power Electronics and Motion Control Conference (IPEMC-ECCE Asia), 2016, pp. 3012-3017, doi: 10.1109/IPEMC.2016.7512776.

[26] Jiancheng Zhang, Youtong Fang, Xiaoyan Huang and Jian Zhang, "Design of in-wheel permanent magnet synchronous motor with concentrated fractional-slot winding and winding switching technology," 2013 International Conference on Electrical Machines and Systems (ICEMS), 2013, pp. 1202-1206, doi: 10.1109/ICEMS.2013.6713366.

[27] X. Yanliang and F. Kaijie, "Parameter Design and Winding Switch Analysis on Driving BDCM Based on the Simulation of Electric Vehicle," 2007 2nd IEEE Conference on Industrial Electronics and Applications, 2007, pp. 2859-2864, doi: 10.1109/ICIEA.2007.4318935.